RSC Advances

ROYAL SOCIETY OF CHEMISTRY

www.rsc.org/advances

Cite this: DOI: 10.1039/c0xx00000x

www.rsc.org/xxxxxx

ARTICLE TYPE

Successful aqueous processing of lead free $0.5Ba(Zr_{0.2}Ti_{0.8})O_3$-$0.5(Ba_{0.7}Ca_{0.3})TiO_3$ piezoelectric material composition

A. Kaushal[a,*], S. M. Olhero[a], B. K. Singh[b], Reza Zamiri[a], V. Saravanan[a] and J. M. F. Ferreira[a,]**

Received (in XXX, XXX) Xth XXXXXXXXX 20XX, Accepted Xth XXXXXXXXX 20XX

DOI: 10.1039/b000000x

We report on successful aqueous processing of lead free piezoelectric $0.5Ba(Zr_{0.2}Ti_{0.8})O_3$–$0.5(Ba_{0.7}Ca_{0.3})TiO_3$ (BZT–BCT) composition with final functional properties of materials unaffected from various processing steps involved. XRD results shows single tetragonal perovskite crystalline phase for as received sintered BZT–BCT powder. The purity of perovskite phase for BZT–BCT powder was found to be controlled even after ageing material composition in water media for 24 h on successful surface treatment against hydrolysis. The aqueous suspension of surface treated BZT–BCT powder with 50 vol. % solid loading was successfully transformed into micro-sized granules via freeze granulation (FG) method. Various structural, electrical and mechanical properties of sintered BZT–BCT–FG and BZT–BCT–NG ceramics consolidated from freeze granulated and non-granulated (NG) powders, respectively, were measured. The dielectric constant (ε_r) values of BZT–BCT–FG sample were found to be higher with lower dielectric loss (tan δ) values in comparison to those of sample prepared from the BZT–BCT–NG powder at all temperatures and frequency ranges tested. Nanoindentation results reveal that the ability to oppose deformation was nearly 10 folds higher for BZT–BCT–FG (6.93 GPa) than for BZT–BCT–NG ceramics (543 MPa). The functional properties of BZT–BCT–FG samples confirmed the benefits of the aqueous processing approach in comparison to the traditional dry pressing.

A Introduction

Successful aqueous processing of multicomponent electroceramics relies on achieving their various functional properties unaffected from the odds of ionic leaching in water. [1, 2] $0.5Ba(Zr_{0.2}Ti_{0.8})O_3$–$0.5(Ba_{0.7}Ca_{0.3})TiO_3$ (hereafter referred to as BZT–BCT) has been reported as an interesting lead free ferroelectric system that exhibits highest piezoelectric coefficient d_{33}~620pC/N and a good candidate material to replace lead based $Pb[Zr_xTi_{1-x}]O_3$ (PZT) piezoelectric ceramics. [3-5] BZT–BCT is a representative dielectric material of high dielectric constants for multilayer ceramic capacitor applications. [6, 7] There have been recent reports in literature on sintering behavior of BZT–BCT material showing dielectric properties at various sintering temperatures. [8-11] Depending on the material's functional applications, one needs to control its structural and compositional evolution to achieve superior properties. Further, the materials need to be consolidated in bulk (polycrystalline ceramics, single crystals) or in films (thick and thin) form to draw benefits from their relevant properties. Reduction in dimension of all passive components without compromising on performance and improved reliability is a necessary trend in electronics technology.

Till date nonaqueous processing of electroceramic is still preferable because of the common water sensitiveness of the starting powders and the consequent leaching of material components, which affects the final product functional properties and often result in exaggerated grain growth and low final density. [12, 13] The reason for the detrimental effects of water is believed to be the instability of alkaline-earth titanates in water, which were firstly observed experimentally on calcium titanate ($CaTiO_3$). [14] However, aqueous processing is attractive from environmental and economical standpoints. The knowledge acquired on aqueous processing of other water sensitive powders such as magnesium aluminate ($MgAl_2O_4$), zirconia-toughened-alumina (ZTA) [15, 16] is likely to be helpful in this pursue. On the other hand, the recently demonstrated feasibility of aqueous processing the BZT–BCT electroceramic powders [17] can be regarded as an important corn stone for designing the necessary experiments aiming at the preparation of high performance granulated powders for dry pressing. The relevant aspects include the surface chemistry of the particles and how to control it through the selection of type and amount of dispersant, and the evolutions of pH and concentrations of leached ionic species with aging time. Preventing the well-known reactivity of BZT–BCT powders with water is a major challenge towards preparing high quality spherical granules from aqueous suspensions. [17] Therefore, it is essential to investigate how the functional properties of a multicomponent oxide material might be affected by hydrolysis or other processing steps involved in aqueous processing. When BZT–BCT particles get in contact with water

molecules they undergo hydrolysis and, in chemical equilibrium, substantial amounts of Ba^{2+} and Ca^{2+} ions should be leached from BZT–BCT, according to reaction as:

$$BZT * BCT + H_2O \rightleftharpoons (B_{1-x_1}ZT * B_{1-x_2}C_{1-y}T)_{(s)} + (x_1 + x_2)Ba^{2+}_{(aq)} + yCa^{2+}_{(aq)} + 2(x_1 + x_2 + y)OH^-_{(aq)} \quad (1)$$

Therefore, protecting BZT–BCT powder particles against hydrolysis and hindering the leaching process of alkaline earth ions as described by Eq. (1) are very exciting issues. [17] These issues are of high relevance for disclosing how the performance of BZT–BCT ceramics can be maximized. The proposed surface treatment, which consists of adding 2 wt.% aqueous solution of aluminium di-hydrogen phosphate, $Al(H_2PO_4)_3$ (Bindal), proved to be effective in preventing hydrolysis of BZT-BCT powders. It has been reported that the assembly of Bindal onto the surface of the ceramic particles occurs through a chemisorption process of $Al(HPO_4)_3^-$ or $Al(PO_4)_3^{2-}$ species. However, the potential harmful effects of the surface protecting agent, which is likely to add some aluminium and phosphate species, need to be studied to better support the claim of an aqueous successful processing. The earlier findings [17] stimulated us undertaking in the present study further research aiming at preparing high quality spherical granules by freeze granulation (FG) from suspensions containing the surface treated powder and assess the potential benefits in terms of the various functional properties of sintered ceramics. The results obtained confirmed aqueous processing as a viable route to obtain lead free functional ceramics with good dielectric properties unaffected, providing that the surface of the particles has been suitably protected against hydrolysis. The superiority of aqueous colloidal processing and freeze granulation approach became more evident when the dielectric properties of ceramics derived from FG were compared to those of ceramics derived from non-granulated (NG) powders. This kind of lead-free ceramics has been regarded with alacrity for their functional relaxor ferroelectric properties and new processing/sintering approaches are being attempted to improve them in comparison to those prepared through conventional methods. [18]

B Experimental

The BZT–BCT powder was synthesized by using conventional solid state reaction from a precursor mixture of high purity $BaCO_3$ (Sigma-Aldrich, Steinheim, Germany), ZrO_2 (Sigma-Aldrich, Steinheim, Germany), TiO_2 (Riedel-de Haen, Sielze, Germany), and $CaCO_3$ (Sigma-Aldrich, Steinheim, Germany). The mixture was firstly dry ball-milled for 1 h, followed by wet ball-milling in ethanol for 2 h to guarantee complete homogenisation, and then dried at 100 ºC. The dried powder was then calcined at 1000 ºC for 4 h, reground by dry ball milling for 2 h, and then heat treated at 1400 ºC for 4 h followed by 1 h dry ball milling to destroy the coarser agglomerates formed upon heat treatments. The as-obtained powder was then attrition milled for 10 h in ethanol at 700 rpm. The aqueous processing of BZT–BCT powder including various steps such as selection of dispersant, ageing effect in water and rheological behaviour has been reported elsewhere. [17] The various parameters such as pH *versus* time, different ions concentrations in aqueous solvent, selection of dispersant, dispersant concentration, surface chemical modification and surface ionic charge were monitored to obtain stable aqueous suspension of BZT–BCT with high solid loadings. In order to avoid selective ionic leaching, di-hydrogen phosphate was used to protect the powder particles. BZT–BCT aqueous suspension of 50 vol. % solid loading was sprayed into liquid nitrogen (-196 ºC) to obtain micro-sized granules by freeze granulation (Power Pro freeze granulator LS-2, Gothenburg, Sweden). 3 wt.% Duramax B1001 was added as binder in the suspension before spray. The granules were then dried at –49 ºC under a pressure of 1×10^{-3} Torr in a freeze-drying system (Labconco, LYPH Lock 4.5, Kansas City, MO) for 72 h. The dried granules were uniaxial pressed in to disc-shaped pallets of 20 mm diameter at a uniaxial pressure of 60 MPa followed by isostatic pressing at 200 MPa aiming at further enhancing the green density of the samples. Finally the samples consolidated from BZT–BCT–FG, BZT–BCT–NG, and centrifuged BZT–BCT powder after aged for 24 h in water under constant stirring (BZT–BCT–CF) were sintered at 1350 ºC for 4 h.

The flow properties (angle of repose ($\overline{\mathbf{AR}}$), Hausner Ratio (HR) and average flow rate (V) through orifice) of FG and NG powders were assessed using batches of 100 g. A Ford cup with a calibrated orifice was fixed at 30 cm from a horizontal surface and filled with the testing powders. The angle of repose ($\overline{\mathbf{AR}}$) was calculated as:

$$\overline{AR_n} = \frac{\alpha_1+\alpha_2}{2}, \quad (2)$$

where, $\boldsymbol{\alpha_1}$ and $\boldsymbol{\alpha_2}$ are basal angle of the formed pile onto the horizontal surface in two opposed sides, and *n* is the number of measurements per data point. The average flow rate (V) through the Ford cup orifice was calculated as:

$$V_n = \frac{W_n}{T_n}, \quad (3)$$

where, W is weight measured in container in time T, and n is the number of measurements per data point. Five measurements were taken per data point. Hausner Ratio (HR) was also calculated using a graduated measuring cylinder (50 ml, 1 ml accuracy). The volumes of powder samples before (V_1) and after hand tapping until constant volume (V_2) over time were measured to calculate HR as:

$$HR_n = \frac{V_{1n}}{V_{2n}}, \quad (4)$$

The crystallinity of the samples was studied using a Rigaku X-ray diffractometer of CuK_α (1.54 Å) radiations in θ–2θ geometry. Pure strain-free silicon was used as instrumental-standard sample to determine instrumental broadening effect factor in order to deduce instrumental inaccuracy in crystallite size calculations from XRD spectra. Bulk density ($\boldsymbol{\rho_{bulk}}$) of various sintered BZT–BCT ceramics were measured in ethylene glycol liquid using Archimedes principle. Three density measurements were performed for each sample. Dilatometry measurements were performed for both FG and NG green compacts using BAHR-Thermoanalyse (Model: Dil 801L). Nanoindentation measurements were performed on a well-polished surface (up to 6 μm diamond suspension) of BZT–BCT ceramic using a three-side pyramidal Berkovich diamond indenter having nominal edge radius 120 nm (faces 65.3º from vertical axis) attached to a fully calibrated nanoindenter ((TTX-NHT, CSM Instruments). The test

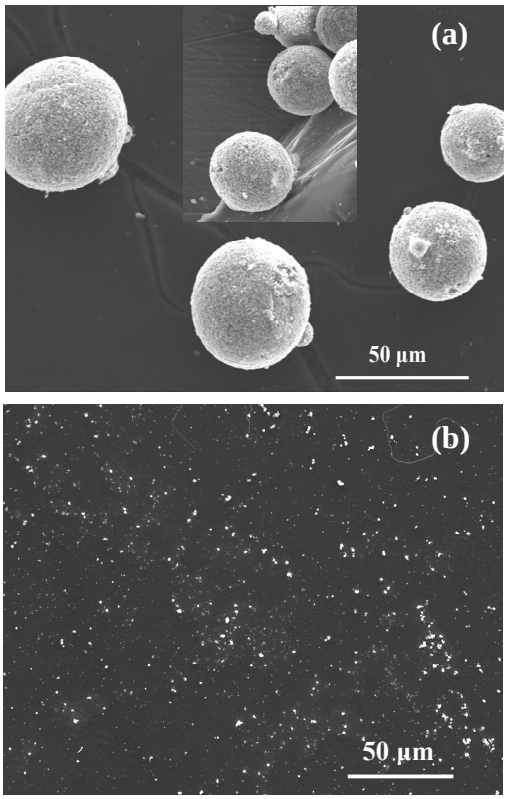

Fig. 1 SEM image of (a) freeze dried green BZT-BCT granules and (b) non granulated BZT-BCT powder. Inset in (a) shows free falling view of granules.

was carried out under progressive multicycle loading with acquisition rate of 10 Hz. The load control to various peak loads in the range 20 to 200 mN with an approach speed of 2000 nm min^{-1} was used. The loading and unloading speed throughout the measurement was kept constant as 30 mN min^{-1} with dwell time of 10 s and pause time of 10 s between each cycle. The microstructure topography of the samples was studied using scanning electron microscopy (SEM) (Hitachi S-4100, Tokyo, Japan). To prevent the charge build up during SEM observations, samples were coated with carbon. For the measurement of electrical properties, sintered samples were polished to the thickness of ~ 0.35 mm and top conductive electrodes were deposited on both sides using silver paste. Dielectric constant and loss were measured at different temperatures and frequencies in the range of 25 ºC to 225 ºC and 100 Hz to 2 MHz respectively, using an impedance analyzer (4294A, Agilent, USA).

C Results and discussion

C.1 Structural properties

Figure 1a shows the SEM images of green BZT–BCT granules obtained after freeze-drying, revealing the successful fabrication of spherical shaped micro-sized BZT–BCT granules. This technique involves spraying well dispersed aqueous suspensions into liquid nitrogen. Quickly freezing the spherical droplets hinders binder segregation and preserves within the granules the high degree of homogeneity achieved in the suspension, contrarily to what happens upon spray drying. Moreover, the granules obtained by FG are massive (not hollow or donut-shaped), softer and less dense, thus being more easily smashed under the external applied pressure and leading to dry powder compacts of high homogeneity. [19] The observed spherical morphology of the granules and their sizes (a few tens of µm) confer to the powder free flowing ability and low friction coefficient with die wall upon dry pressing BZT–BCT compacts.[20] The free flowing ability is strongly conveyed by the image of BZT–BCT granules (inset in the figure) taken at the edge of conducting tape. Moreover, the size distribution of spherical granules was relatively narrow; varying essentially within the range of 25–75 µm. SEM image of non-granulated BZT-BCT powder after 10 h attrition milling in ethanol is shown in Fig. 1b. To enable a good observation of the separated particles, the starting suspension used to prepare the sample for SEM has to be enough diluted. This is the reason why the SEM micrograph is not much crowded with particles. The shape of the particles is relatively isometric and their sizes are distributed according to different populations.

Free-flowing behaviour of FG powder was further confirmed by performing powder rheology for both FG and NG powders. The values of angle of repose ($\overline{\mathbf{AR}}$), Hausner ratio (HR) and average flow rate (V) through orifice calculated from powder rheology tested are listed in Table 1. The results confirmed the excellent flow behaviour of the FG powder that contrasts with that of NG powder. The average flow rate for FG was found to be V = 3.5 ± 0.36 g s^{-1} whereas for NG it could not be determined (the NG powder stacked inside the Ford cup and no flow took place). Therefore, determining the $\overline{\mathbf{AR}}$ in this case required mechanically assisted poring of the NG powder. The $\overline{\mathbf{AR}}$ measurements revealed a lower value for the FG powder ($\overline{\mathbf{AR}}$ = 30 ± 1.5 º) in comparison to that of NG powder ($\overline{\mathbf{AR}}$ = 52 ± 0.5 º) and the conical pile obtained in this last case was too irregular in shape. The Housner ratio was determined using a fixed volume (40 ml) of powders. The HR value measured for FG powder was significantly lower (1.11 ± 0.01) than that obtained for NG powder (1.65 ± 0.02). However, the required weight of FG powder (52.36 ± 0.21 g) was found to be lower when compared to that of NG powder (59.67 ± 0.14 g). These differences depict the typically lower density of FG spherical granules and their regular sizes that hinder interstitial voids being filled with smaller particles, contrasting with NG powder in which particle rearrangements gradually reduce the apparent volume. The lower density of FG granules can easily be understood considering the absence of capillary forces (shrinkage) during ice sublimation. The same reasons also hinder the segregation of processing

Table 1 Various calculated values of $\overline{\mathrm{AR}}$, HR and V for FG and NG powders.

Powder sample	$\overline{\mathbf{AR}}$ (º)	V (g s^{-1})	HR
BZT-BCT-NG	52 ± 0.5	--	1.65 ± 0.02
BZT-BCT-FG	30 ± 1.5	3.5 ± 0.36	1.11 ± 0.01

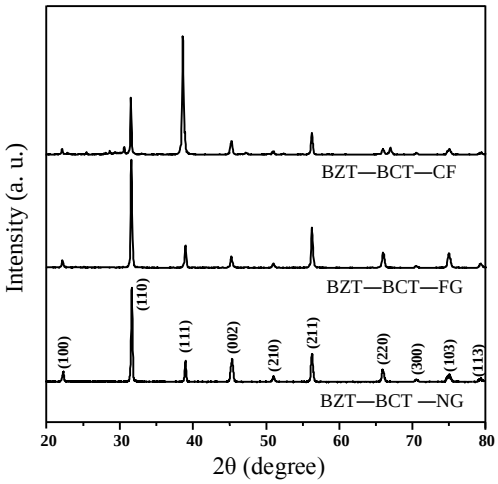

Fig. 2 XRD pattern of BZT–BCT–NG, BZT–BCT–FG and BZT–BCT–CF ceramic samples sintered at 1350 ºC for 4 h.

additives, making FG powders more homogeneous in comparison to granules prepared by spray drying. These features are expected to grant uniform mould filling and homogeneous packing of FG powder upon dry pressing.

Figure 2 shows the room temperature XRD pattern of BZT–BCT ceramics sintered at 1350 ºC for 4 h, derived from non-granulated powder before (BZT–BCT–NG) and after ageing in water for 24 h (BZT–BCT–CF). It is evident that after solid state reaction and milling, the BZT–BCT–NG powder consists of single tetragonal perovskite phase. The diffraction peaks were indexed to the perovskite-type tetragonal structure with space group (*P*4*mm*) in agreement with the respective Joint Committee on Powder Diffraction Standards (JCPDS) card no 05-0626. [21] However, a completely different result was obtained for BZT–BCT–CF ceramics derived from the same powder but after aging in water for 24 h under constant stirring. In this last case, XRD pattern shows extra impurity phase diffraction peaks along with pure tetragonal phase. As a matter of fact, it has been reported that processing of BZT–BCT in aqueous media results in its hydrolysis and non-stoichiometric dissolution reactions which will alter the composition of BZT–BCT powder.[17] Therefore, water sensitive particles need to be surface protected against hydrolysis, [15-17] contrasting with the desired XRD phase purity identified for BZT-BCT-FG ceramics sintered under the same heat treatment schedule, which underwent aqueous processing, as shown in Fig. 2. As a matter of fact, a close matching to phase structure and the absence of impurity peaks (as depicted from XRD pattern) are observed for both BZT–BCT–NG and BZT–BCT–FG ceramics. This means that the desired purity of BZT-BCT composition was not altered upon colloidal processing in aqueous media when the surface of the particles was protected against hydrolysis. These observations enable concluding that no external contamination has been apparently introduced along the preceding processing steps (deagglomeration/milling) in aqueous media. For a deeper analysis, the *a*- and *c*-axis lattice parameters were calculated from the XRD patterns of BZT–BCT–FG and BZT–BCT–NG ceramic samples with tetragonal phase structure.[22] The values of *a*-axis were found to be equal to 4.001 Å and 4.002 Å for BZT–BCT–NG and BZT–BCT–FG, respectively, whereas the corresponding calculated *c*-axis values were 4.004 Å and 4.006 Å. According to these values, the calculated *c/a* ratios are 1.0008 and 1.0011 for BZT–BCT–NG and BZT–BCT–FG ceramic materials, respectively. This small difference reveals that the tetragonality of perovskite structure was not much distorted.

To gain further insights, the crystallite sizes of FG and NG samples were calculated from XRD data using Hall-Williamson method. Scherrer equation does not take into account of the broadening due to lattice strain present in the sample. Generally, the integral breadth of XRD peak is given by the integrated intensity divided by the maximum intensity. Thus, the observed peak broadening B_o may be represented as

$$\boldsymbol{B_r = B_0 - B_i} \qquad (5)$$

where B_0 is the observed peak broadening in radians, B_i is the instrumental broadening in radians and B_r is the broadening due to the small crystallite size and lattice strain. The instrumental broadening has been estimated using a pure strain-free silicon standard subject to XRD under identical conditions. According to Scherrer equation [22] the broadening due to small crystallite size may be expressed as [23]:

Table 2 Calculated values of densities, linear shrinkage, crystallite sizes and lattice axis parameters for various BZT-BCT ceramics sintered at 1350 ºC.

Samples	$\boldsymbol{\rho_{green}}$ (g cm^{-3})	$\boldsymbol{\rho_{bulk}}$ (g cm^{-3})	$^{*}\boldsymbol{\rho_{relative}}$ (%)	Linear shrinkage (%)	*a*-axis length (Å)	*c*-axis length (Å)	*c/a* ratio	Crystallite size (nm)
BZT–BCT–NG	2.79 ±0.193	5.155 ±0.196	93.95 ± 3.45	10.38 ± 0.04	4.001	4.004	1.0008	34.18 ± 2.8
BZT–BCT–FG	2.87 ±0.102	5.310 ±0.126	96.77 ± 2.29	15.21 ± 0.08	4.002	4.006	1.0011	40.77 ± 1.57
BZT–BCT–CF	2.84 ±0.183	5.216 ±0.214	95.06 ± 3.57	12.61 ± 0.02	-	-	-	-

[*]Theoretical value of particle density used for relative density calculation was measured to be 5.487 g cm^{-3} using Multi Pycnometer (Quanta Chrome, USA)

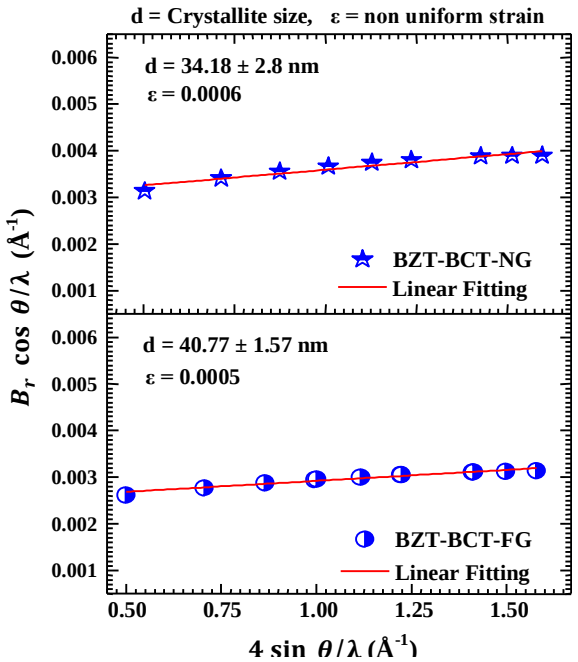

Fig. 3 A typical Hall–Williamson plot for BZT–BCT-NG and BZT–BCT-FG ceramics sintered at 1350 ° C for 4 h.

$$B_c = \frac{k\lambda}{d\cos\theta} \qquad (6)$$

where B_c is the broadening solely due to small crystallite size, k a constant whose value depends on particle shape and usually taken as unity, d the crystallite size, θ is the Bragg angle and λ is the wavelength of incident X-ray beam (1.5418 Å). Similarly, according to Wilson [24] the broadening due to lattice strain is expressed as

$$B_s = 4\varepsilon\tan\theta \qquad (7)$$

where B_s is the peak broadening due to lattice strain and ε the strain distribution within the material and θ is the Bragg angle. Thus the total broadening of the peak is given as the sum of Eqs. (6) and (7) excluding the instrumental broadening which can be expressed as:

$$B_r = \frac{k\lambda}{d\cos\theta} + 4\varepsilon\tan\theta \qquad (8)$$

Or

$$\frac{B_r\cos\theta}{\lambda} = \frac{k}{d} + \varepsilon\frac{4\sin\theta}{\lambda} \qquad (9)$$

The plot of $(Br\cos\theta)/\lambda$ *versus* $(4\sin\theta)/\lambda$ is a straight line with slope equal to ε and hence the crystallite size *d* can be estimated from the intercept. A typical Hall–Williamson plot for BZT–BCT sintered samples when consolidated from NG and FG BZT–BCT powders are shown in Fig. 3. An increase of crystallite size from 34.18 ± 2.8 nm to 40.77 ± 1.57 nm was calculated for sintered BZT–BCT ceramics consolidated from NG and FG BZT–BCT powders, respectively. The observed differences suggest that the diffusion paths have been shortened in the samples derived from the FG powder due to their higher degree of homogenization. [25]

Generally, micron-sized granules obtained by freeze granulation exhibit a number of favourable features in comparison to loose powders or granules obtained by spray drying as follows: (i) lower green density in comparison to granules obtained by spray drying; (ii) are homogeneous (no binder segregation occurs); (iii) free-flowing behaviour that enables their spatial rearrangements; and (iv) are easily smashed under the applied pressure. These features favour the elimination of the intergranular pores. [26] The binder in FG granules acts as lubricant, assisting primary particles sliding and rearranging to increase the packing efficiency and compact density. This explains why the green density of FG compacts is higher in comparison to that of NG ones (as shown in Table 2). An increase in green density will enhance the densification ability upon sintering while implying a decrease of total shrinkage. This is confirmed by the data plotted in Fig. 4 that compares the dilatometric curves of FG and NG green bodies measured from room temperature to 1370 ºC. It can be clearly seen that the shrinkage starts earlier and progresses at a much faster rate for the FG powder in comparison to the NG one. Essentially, diverging lines that do not deviate much from horizontality can be observed up to ~1100 ºC and ~1200 ºC for FG and NG samples, respectively. The positive inclination observed for NG sample reveals that thermal expansion predominates over any shrinkage, while the FG samples exhibits a negative inclination along the lower temperature range, probably due to the homogeneous distribution of the particles and the burnout of binder among them that enables them to gradually approach each other. The benefits of freeze granulation here are very evident, being translated by a downshift of the onset of shrinkage of >100 ºC. For the FG sample, the shrinkage becomes very fast for T ≥ ~1100 ºC, achieving the maximum shrinkage rate at ~1200 ºC, whereas for NG sample at higher temperature (1300 ºC) exhibits a shrinkage rate similar to that of FG sample at 1150 ºC. For the FG sample, the maximum density has apparently been achieved at about ~1240 ºC with a slop reversion of dilatometric curve, while the densification process of NG sample was still far from completion at 1370 ºC. The dilatometric curves plotted in Fig. 4 are consistent with the results of relative density measured for the sintered samples (Table 2). The highest relative density (96.77 ± 2.29 %, based on the density of synthesized BZT–BCT = 5.487 g

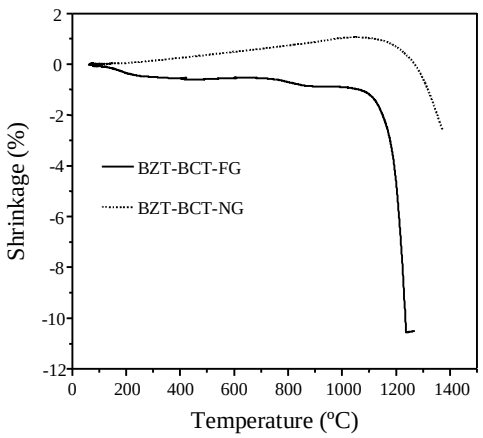

Fig. 4 Dilatometric behaviour of BZT-BCT-FG and BZT-BCT-NG green compacts.

cm^{-3} measured by helium pycnometry) was obtained for BZT–BCT–FG ceramics, whereas a significantly lower value (93.95 ± 3.45 %) was achieved for BZT–BCT–NG ceramics. The experimental value of powder density (5.487 g cm^{-3}) measured from helium pycnometry was found to be lower than the theoretical density value (5.77 g cm^{-3}) of BZT–BCT powder. The lower measured density could be due to the effects of 10 h attrition milling on the structure of the outer surface layer of the particles. It is known that severe milling increases lattice stress/strain and often enhances the amorphous fraction.

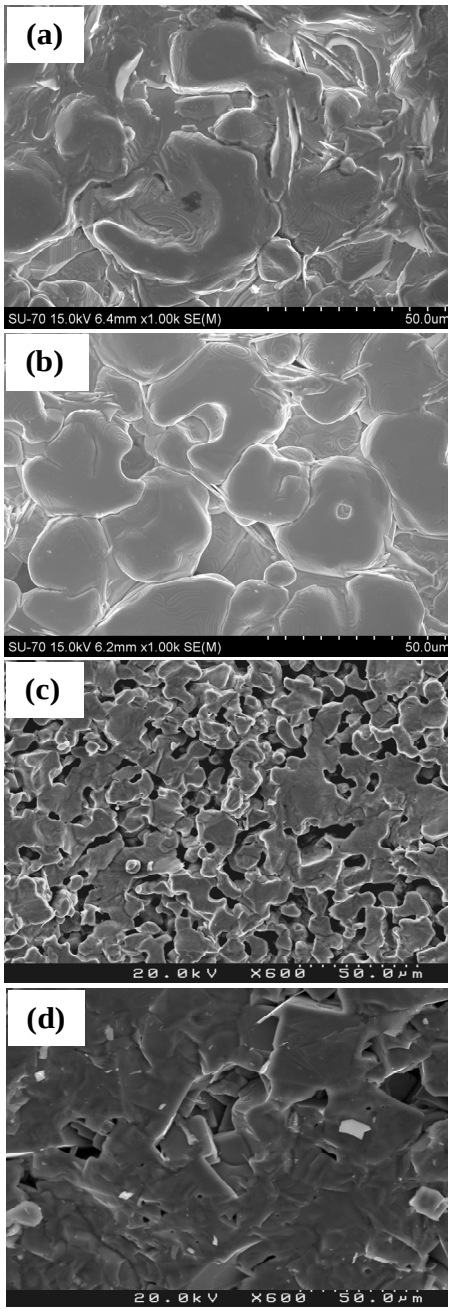

Fig. 5 SEM images of external surfaces (a) BZT–BCT–NG and (b) BZT–BCT–FG ceramics sintered at 1350 ºC with corresponding surface fractures images shown in (c) and (d) respectively.

Figure 5(a)-(b) shows SEM images of external surfaces of sintered BZT–BCT–NG and BZT–BCT–FG ceramics respectively. The corresponding images of surface fractures are shown in Fig. 5(c)-(d). These SEM images reveal different morphological features that reflect the different sintering abilities of BZT–BCT–FG and BZT–BCT–NG powders. Fig. 5 (c) clearly shows that the porosity fraction of BZT–BCT–NG sample is higher than that of BZT–BCT–FG one, in good agreement with the bulk density data determined by immersion method (Table 2), as well as with the measured geometrical density values, 4.84 ± 0.21 g cm^{-3} and 4.61 ± 0.23 g cm^{-3} for FG and NG ceramics, respectively. The geometrical density values are lower than the corresponding values obtained by the immersion method as 5.310 ± 0.126 g cm^{-3} and 5.155 ± 0.196 g cm^{-3} for FG and NG ceramics, respectively. The differences are attributed to the presence of open pores that increase the apparent volume in geometrical assessment. Therefore, measuring the sintered density by both methods enables to have a better idea about the influence of open porosity. It is also clear that the grain size for BZT–BCT–FG ceramics is noticeable larger than that of BZT–BCT–NG ceramics, Fig. 5c-d.

C.2 Hardness

The hardness (H) of the material is defined as the ratio of the peak load, P_{max}, to the projected area under nanoindentaion, A_c, i.e.,

$$H = P_{max}/A_c\,, \qquad (10)$$

However, the projected area under nanoindenter depends on the contact depth, h_c, which in turn depends on the shape of the indenter. In case of Berkovich nanoindentar (used in present study), A_c is estimated to be $24.5\ h_c^2$. Further, according to Oliver and Pharr analysis [27] the contact depth can be determined using equation as:

$$h_c = h_{max} - 0.75\,P_{max}/S, \qquad (11)$$

where, h_{max} is the displacement at peak load and S is the initial

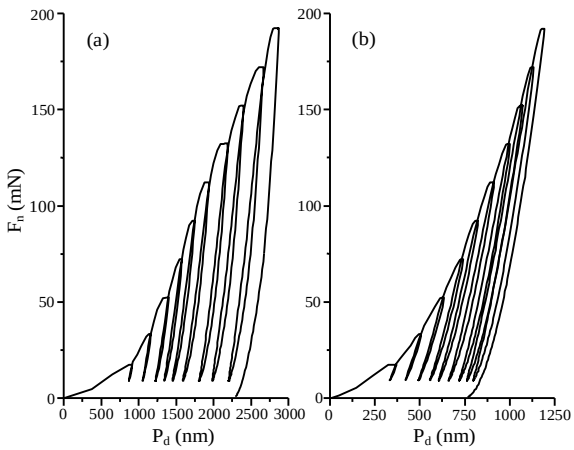

Fig. 6 Load *versus* displacement curve used for (a) BZT–BCT–NG and (b) BZT–BCT–FG ceramics sintered at 1350 ºC.

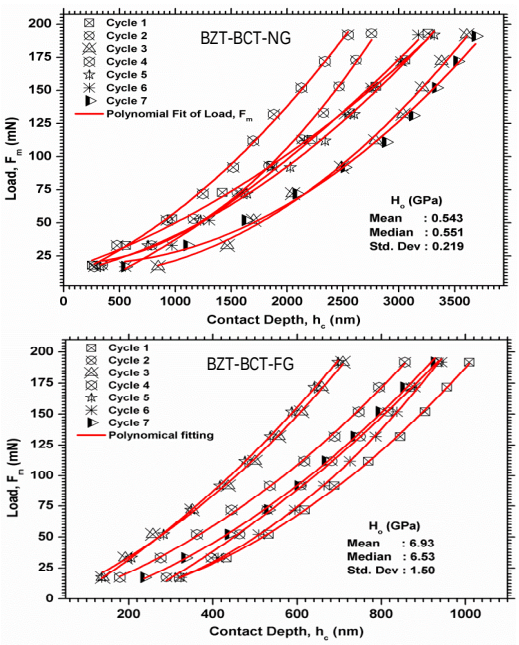

Fig. 7 Variation of contact depth (h_c) with peak load (F_m) along each indentation cycle for BZT-BCT-NG and BZT-BCT-FG ceramics sintered at 1350 ºC.

unloading stiffness expressed as *dP/dh* and can be calculated from the slope of the unloading segment of the load-displacement curve. Seven different imprints were made at various places and aggregated values were used for analysis using standard Oliver and Pharr method. [27] Figure 6 (a&b) shows a typical load *versus* displacement curve used for the BZT–BCT–NG and BZT–BCT–FG ceramics, respectively. Large displacement values were observed for BZT–BCT–NG ceramics when compared with displacement values of BZT–BCT–FG ceramics under application of same load. The lower displacement values observed for the BZT–BCT–FG ceramic reflects the higher stiffness of sintered microstructure derived from compacted freeze granulated powders.

The indentation size, *D*, which is proportional to the value of contact depth, h_c is related to the peak load as: [28]

$$P = a_0 + a_1 h_c + a_2 h_c^2, \quad (12),$$

where, $a_0, a_1 \; and \; a_2$ are constant parameters. Further, the parameter a_2 is considered as a measure of the load-independent hardness H_0 and related to the empirical formula given by: [28]

$$H_0 = k a_2 \quad (13),$$

where, k is a constant which depends on the indenter geometry. For Berkovich indenter, the value of k is 1/24.5. Figure 7 shows the variation of contact depth h_c with peak load for each indentation cycle. The curve was fitted with polynomial function (equation 12) and the fitted value for $a_0, a_1 \; and \; a_2$ are shown in Table 3. From the best fitting of experimental results to equation (12), the calculated ability to oppose the deformation for the BZT–BCT–NG ceramics (543 MPa) was found to be nearly 10 folds less than that of BZT–BCT–FG ceramics (6.93 GPa). This significant difference is probably due to the higher number of pores observed in the fracture surface of BZT-BCT-NG ceramic in comparison to that of BZT-BCT-FG one. Pores may lead to large displacements of the indenter under the same load.

C.3 Electrical properties

Another aim of the present work is to evaluate if aqueous processing steps negatively affect the electrical properties of sintered BZT–BCT–FG in comparison to BZT–BCT–NG ceramics. Namely, it was hypothesized that the Al and P elements coming from the thermal decomposition of the surface protecting agent $Al(H_2PO_4)_3$ could interfere with the perovskite structure and properties of BZT–BCT.

Figure 8a&b shows the temperature dependences of ε_r and tan δ within the range from 25 – 225 ºC measured at constant frequency of 10 kHz. It can be seen that all the evaluated ceramics exhibit a maximum dielectric constant ($\varepsilon_{r_{max}}$) at 95 ºC, corresponding to the phase transition temperature (T_c) for $0.5Ba(Zr_{0.2}Ti_{0.8})O_3–0.5(Ba_{0.7}Ca_{0.3})TiO_3$ composition (Fig. 8a). The corresponding dielectric loss data plotted in Fig. 8(b) reveals maxima values at the proximity of T_c. At T_c, frequency of the soft mode tends to zero and the lattice displacement associated with it becomes unstable and leads to phase transition. [29] The superiority of aqueous colloidal processing and freeze granulation approach becomes more evident when the dielectric properties of ceramics

Table 3 Values of various constant parameters calculated from h_c *vs* F_m plot (figure 7)

Indentation cycles	BZT-BCT-NG				BZT-BCT-FG			
	a_1	a_2	a_3	Adj. R-Square	a_1	a_2	a_3	Adj. R-Square
Cycle 1	14.06484	0.02816	7.82315E-6	0.99659	-7.04261	0.01898	1.75425E-4	0.99924
Cycle 2	19.56167	0.00313	2.33352E-5	0.99431	-33.64236	0.13383	1.15816E-4	0.99855
Cycle 3	9.77102	0.00281	1.46819E-5	0.99442	-0.92531	0.13572	1.89491E-4	0.99721
Cycle 4	8.31665	0.03483	1.50264E-5	0.99657	-3.70724	0.09405	1.55857E-4	0.99860
Cycle 5	11.18406	0.01837	1.11452E-5	0.99729	-10.86676	0.18112	1.59953E-4	0.99972
Cycle 6	-7.72655	0.03759	7.61056E-6	0.99713	-2.51254	0.01347	2.35983E-4	0.99899
Cycle 7	19.36415	0.00476	1.34925E-5	0.99306	-10.46316	0.07656	1.56675E-4	0.99869

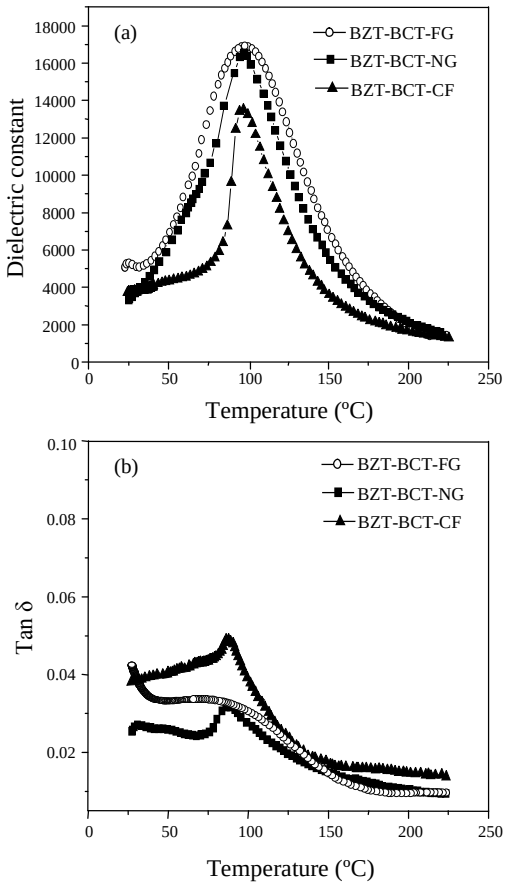

Fig. 8 Temperature dependences of (a) dielectric constant (ε_r) and (b) dielectric loss (tan δ) values within the range from 25 – 225 ºC at constant frequency of 10 kHz measured for prepared BZT-BCT ceramics sintered at 1350 ºC.

derived from FG are compared to those of ceramics derived from NG powders. Two obvious phase transitions above 25 ºC corresponding to the orthorhombic–tetragonal and tetragonal–cubic, respectively, were observed for both BZT–BCT–NG and BZT–BCT–FG ceramics.[3] However, BZT–BCT–CF (non-treated powder kept for 24 h in aqueous media under constant stirring) shows significant differences in dielectric response and electrical behavior as only one phase transition was observed for BZT–BCT–CF ceramic as shown in Fig. 8a. The absence of phase transition at low temperature in case of BZT–BCT–CF ceramic reflects the chemical phase impurities due to hydrolysis (Fig. 2). Moreover, the value of ε_r at room temperature (30 ºC) was found to be higher for BZT–BCT–FG ceramics (ε_r ~ 4984) when compared with values measure for BZT–BCT–NG (ε_r ~ 3557) and BZT–BCT–CF (ε_r ~ 3409). Furthermore, the tan δ *versus* T plots (Fig. 8b) show small loss (tan δ values) for BZT–BCT–FG ceramics along the entire temperature range tested. The values of ε_r and tan δ obtained for various BZT–BCT sintered ceramics are illustrated in Table 4. The observed higher $\varepsilon_r$value measured for BZT–BCT–FG can be attributed to the enhanced homogeneity of BZT–BCT ceramics derived from the FG powder due to the higher compaction degree of the green bodies and their better sintering ability in comparison to those derived from the NG BZT–BCT powder. It can be concluded

Table 4 Measured dielectric constant (ε_r) and dielectric loss (tan δ) values for various BZT-BCT ceramics sintered at 1350 ºC

Samples	ε_r	tan δ
BZT–BCT–NG	3557	0.027
BZT–BCT–FG	4984	0.035
BZT–BCT–CF	3409	0.037

that, the treatment of the powder strongly affects the dielectric properties, not only the losses that would be expected, but also the real part. If not treated, as in case of BZT-BCT-CF ceramic, only one phase transition in dielectric responses at higher T_c can be found with higher loss values in comparison to that of FG ones, revealing the efficacy of treatment.

Figure 9 shows the frequency dispersion of real (ε′) and imaginary (ε″) part of dielectric constant values of BZT–BCT ceramics prepared at different conditions in the range from 100 Hz to 1 MHz. For all samples, the ε′ and ε″ values decrease with increasing frequency, a commonly observed behaviour for dielectric/ferroelectric materials. The fall in dielectric constant arises from the fact that polarization does not occur instantaneously with the application of the electric field as charges possess inertia. The delay in the response towards the impressed alternating electric field at high frequencies leads to loss and hence decline in dielectric constant. The higher values of ε′measured for BZT–BCT–FG ceramic compared to ε′values of BZT–BCT–NG ceramic in all frequency range tested which could be attributed to the resulted high dense ceramic on sintering of BZT–BCT–FG material. The high ε_r values associated with the low tan δ ones (Fig. 8) leads to lower values of ε″ for BZT–BCT–FG ceramic when compared to ε″ values measured for BZT–BCT–NG ceramics as shown in Fig. 9. For BZT–BCT–NG ceramics, the decrease in grain size and the concomitant increasing number of grain boundaries resulted in lower polarization intensity and therefore in lower ε_r values. [30] In addition, Cole-Cole plot for the prepared samples has also been included in the inset of Fig. 9. The Cole-Cole equation for complex permittivity can be written as:

$$\varepsilon^* = \varepsilon' + i\varepsilon'' = \varepsilon_\infty + \frac{\varepsilon_s - \varepsilon_\infty}{1+(i\omega\tau)^{1-\alpha}} - i\frac{\sigma_{dc}}{\varepsilon_0\omega} \qquad (14)$$

where, ε_s and ε_∞ are the dielectric constants on low and high frequency sides of the relaxation, ω is the angular frequency ($\omega = 2\pi f$), τ is the relaxation time, α indicates the width of relaxation time distribution and provides a measure of the polydispersive nature. The second term in the equation is due to high conducting behaviour contributing only to ε″. Assuming a single relaxation time τ, the variation of ε_r with ω is given by the Debye equation as,

$$(\varepsilon_r - \varepsilon_\infty)/(\varepsilon_s - \varepsilon_\infty) = (1 - j\omega\pi)/(1 + \omega^2\tau^2), \qquad (15)$$

This gives the relation for the ε′ and ε″ at high frequency as [31]

$$\varepsilon' = \varepsilon_\infty + (\varepsilon_s - \varepsilon_\infty)/(1 + 4\pi^2 f^2 \tau^2), \qquad (16)$$

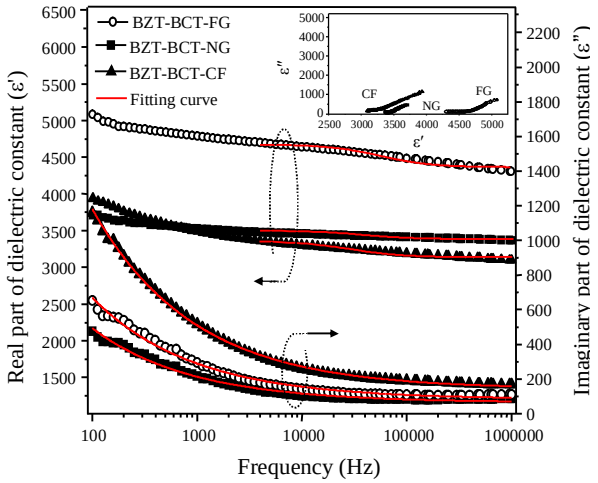

Fig. 9 Real (ε′) and imaginary (ε″) part of dielectric constant values of BZT–BCT ceramics in the frequency range from 100 Hz to 1 MHz measured for various BZT–BCT ceramics sintered at 1350 ºC. Inset shows corresponding Cole-Cole plot.

$$\varepsilon'' = 2\pi f \tau (\varepsilon_s - \varepsilon_\infty)/ (1 + 4\pi^2 f^2 \tau^2) \quad (17)$$

The associated dielectric parameters, ε_∞, ε_s and τ were evaluated by fitting ε' *versus* frequency variation in high frequency region with equation (16) as shown in Fig. 9. The various fitting parameters are listed in Table 5. An increase in the value of ε_∞ (4359.056) as well as ε_s (4643.406) for BZT-BCT-FG ceramic was observed when compared to corresponding values measured for BZT-BCT-NG ceramic (ε_∞ = 3386.63; ε_s = 3462.918). Moreover, the measured values are even lower for the BZT-BCT-CF sample, meaning that besides granulation, the surface treatment also matters. This is an obvious consequence of stoichiometric deviations due hydrolysis occurring during the aging period in water in the case of non-surface treated sample. The variation of ε'' with frequency at room temperature was fitted with power equation given by Jonscher, as $\varepsilon'' \propto f^{n-1}$, where, $0 \leq n \leq 1$. [32] The value of exponent n, obtained after fitting as shown in Fig. 9 are also listed in Table 5. A slight increase in the exponent n was found for the BZT-BCT-FG ceramic when compared to BZT-BCT-NG ones. It has been suggested [33] that further improvements on dielectric loss BZT–BCT ceramics can be obtained by adding MgO and Al_2O_3 as additives. Further, varying the Zr/Ti and Ba/Ca ratios in the solid solution has also been pointed out as a way for tailoring the dielectric constant for tunable capacitor applications. [33]

Conclusions

Micro-sized granules of lead free BZT–BCT piezoelectric material via freeze granulation method were successfully fabricated via spraying a stable aqueous suspension into liquid nitrogen (freeze granulation), followed by freeze drying. The results obtained enable concluding that freeze granulation enhances the packing ability of the powder and enables achieving higher levels of green density and homogeneity in green compacts, features that improve the sintering ability and the overall properties of sintered ceramics. The consistency of functional properties such as phase transition temperatures of BZT–BCT–FG ceramics with those of BZT–BCT–NG ceramics shows that the material is not negatively affected by the surface treatment given to the BZT–BCT powder to protect it against hydrolysis. The results also showed that aqueous processing of non-surface treated BZT–BCT powder leads to the formation of impurity phases derived from the non-stoichiometric cationic leaching when the powder is dispersed in water. These hydrolysis reactions degrade the functional properties of the resultant BZT–BCT ceramics.

Table 5 Various fitting parameters obtained from fitting frequency dispersion behaviour of real and imaginary part of dielectric constant (Fig. 9)

Samples	ε_∞	ε_s	τ	n
BZT-BCT-NG	3386.637	3462.918	2.83E-06	0.54014
BZT-BCT-FG	4359.056	4643.406	1.95E-06	0.54714
BZT-BCT-CF	3132.525	3318.082	3.45E-06	0.54962

Acknowledgments

Authors, A. Kaushal, S.M. Olhero, B. K. Singh, Reza Zamiri and V. Saravanan would like to thank the Foundation for Science and Technology of Portugal (FCT) for the financial support under the grant references SFRH/BPD/77598/2011, SFRH/BPD/87486/2012, SFRH/BPD/76184/2011, SFRH/BPD/76185/2011 and SFRH/BPD/80742/2011, respectively. The authors would also like to thank CICECO for the work at the University of Aveiro and FCT for the financial support under the project PTDC/CTM/099489/2008.

Notes and references

[a] *Department of Materials and Ceramic Engineering, CICECO, University of Aveiro, 3810-193, Aveiro-Portugal. Fax: +351–234–370204; Tel.: +351–234–370354;*

[b] *Department of Mechanical Engineering and TEMA, University of Aveiro, 3810-193, Aveiro-Portugal*

** E-mail: ajay.kaushal@ua.pt ; ** E-mail: jmf@ua.pt*

1 A. Neubrand, R. Lindner and P. Hoffmann, *J. Am. Ceram. Soc.*, 2000, **83 [4]**, 860.
2 J.M.F. Ferreira, S.M. Olhero and A. Kaushal, *J. Eur. Cer. Soc.*, 2013, **33**: 2509.
3 W. Liu and X. Ren, *Phys. Rev. Lett.*, 2009, **103**, 257602.
4 W. Yugong, H. Zhang, Y. Zhang, M. Jinyi and X. Daohua. *J. Mater. Sci.*, 2003, **38**, 987.
5 T. Takenaka and H. Nagata, *J. Eur. Ceram. Soc.*, 2005, **25**, 2693.
6 V.S Puli, A. Kumar, D.B. Chrisey, M. Tomozawa, J.F. Scott and R.S. Katiyar, *J. Phys. D: Appl. Phys.*, 2011, **44**, 395403.
7 V.S. Puli, D.K. Pradhan, W. Pérez and R.S. Katiyar, *J Phys. and Chem. of Solids*, 2013, **74**, 466.
8 P. Mishra, Sonia and P. Kumar, *J. Alloys Compd.*, 2012, **545**, 210.
9 H. Bao, C. Zhou, D. Xue, J. Gao and X. Ren, *J. Phys. D: Appl. Phys.*, 2010, **43**, 465401.
10 S. Su, R. Zuo, S. Lu, Z. Xu, X. Wang and L. Li, *Curr. Appl. Phys.*, 2011, **11**, S120.
11 B. Li, J.E. Blendell and K.J. Bowman, *J. Am. Ceram. Soc.*, 2011, **94**, 3192.

12 D.A. Anderson, J.H. Adair, D. Miller, J.V. Biggers and T.R. Shrout, Surface Chemistry Effects on Ceramic Processing of BaTiO3 Powder. pp. 485–92 in Ceramic Transactions, Vol. 1, Ceramic Powder Science II, A. Edited by G. L. Messing, E. K. Fuller Jr., and H. Hausner. *Am. Ceram. Soc.*, Westerville, OH, 1988.

13 P. Nanni, M. Leoni, V. Buscaglia and G. Aliprandi, *J. Eur. Ceram. Soc.*, 1994, **14**, 85.

14 H.W. Nesbitt, G.M. Bancroft, W.S. Fyfe, S.N. Karkhanis, A. Nishijima, *Nature*, 1981, **289**, 358.

15 S.M. Olhero, I. Ganesh, P.M. Torres, J.M.F. Ferreira. *Langmuir*, 2008, **24**, 9525.

16 S.M. Olhero, I. Ganesh, P.M.C. Torres, F.L. Alves and J.M.F. Ferreira, *J. Am. Ceram. Soc.*, 2009, **92**, 9-16.

17 A. Kaushal, S.M. Olhero and J.M.F. Ferreira, *J. Mater. Chem. C*, 2013, **1**, 4846.

18 S. Mahajan, O.P. Thakur, D.K. Bhattacharya and K. Sreenivas, *Mater. Chem. Phys*., 2008, **112**, 858.

19 B. Nyberg, E. Carlstrom and R. Carlsson, Freeze granulation of liquid phase sintered silicon carbide pp 107-113 in Ceramic transaction, vol. 42, Silicon-Based Structural Ceramics, Edited by Brian W. Sheldon and Stephen C. Denforth, *Americal Ceramic Society*, Westerville, Ohio, 1994.

20 H.A. Janssen, *Zeit d Vereins Deutsch Ing*., 1895, **39**, 1045.

21 *Joint Committee on Powder Diffraction Standards (JCPDS)* card no 05–0626.

22 M.F.C. Ladd and R.A. Palmer, Structure Determination by X-ray Crystallography, 3rd ed., Plenum Press, New York, 1993.

23 B.D. Cullity and S.R. Stock, Elements of X-Ray Diffraction, third ed. New Jersey: Prentice Hall, 2001.

24 J.t. Langford, A.Wilson, *J. Appl. Crystallogr*., 1978, **11 (2)**, 102.

25 A. Kaushal**,** S.M. Olhero, P. Antunes, A. Ramalho and J.M.F. Ferreira, *Mater. Res. Bull*., 2014, **50**, 329.

26 J. Zheng and J S. Reed, *J. Am. Ceram. Soc.*, 1988, **71 (11)**, C456.

27 W.C. Oliver, G.M. Pharr, *J. Mater. Res*., 2004, **19**, 3.

28 J. H. Gong, J. J. Wu and Z. D. Guan, *J. Eur. Ceram. Soc*., 1999, **19**, 2625.

29 E. Tasarkuyu, A. Coskun, A.E. Irmark, S. Akturk, G. Unlu, Y. Samancioglu, A. Yucel, C. Sarikurkcu, S. Aksoy and M. Acet, *J. Alloys Compd*., 2011, **509**, 3717.

30 F. Yan, P. Bao, H.L.W. Chan, C.L. Choy and Y. Wang, *Thin Solid Films*, 2002, **406**, 282.

31 M Davies, *"Some electrical and optical aspects of molecular behaviour"*. Pergamon Press London*:* 1965; Vol. 337

32 A. K. Jonscher, *"Dielectric Relaxation in Solids"* Chelsea Dielectrics press: London, 1983.

33 X.G. Tang and H.L.W. Chan, *J. Appl. Phys*., 2005, **97**, 034109.